High speed infrared camera diagnostic for heat flux measurement in NSTX

J.-W. Ahn,[1] R. Maingi,[1] D. Mastrovito,[2] and A. L. Roquemore[2]
[1]*Oak Ridge National Laboratory, Oak Ridge, Tennessee 37831, USA*
[2]*Princeton Plasma Physics Laboratory, Princeton, New Jersey 08543, USA*

(Received 5 August 2009; accepted 2 January 2010; published online 3 February 2010)

A new high speed infrared camera has been successfully implemented and produced first set of heat flux measurements on the lower divertor tiles in the NSTX tokamak. High spatial and temporal resolutions, 6.4 mm and 1.6–6.3 kHz, respectively, enable us to investigate detailed structure of heat flux deposition pattern caused by transient events such as edge localized modes. A comparison of the data with a slow infrared camera viewing the same region of interest shows good agreement between the two independent measurements. Data analysis for various plasma conditions is in progress. © *2010 American Institute of Physics.* [doi:10.1063/1.3297899]

I. INTRODUCTION

Spherical tokamaks have smaller plasma volume for a given major radius relative to conventional tokamaks, leading to a higher heat flux density on the divertor plates for a given input power. Heat flux scaling is an important research topic both for extrapolation to next step devices such as NHTX and ITER and for divertor design of planned NSTX upgrades. Two standard frame rate (30 Hz) infrared (IR) cameras[1] have been operated to measure heat flux both onto upper and lower divertor tiles in NSTX since 2002.[2,3] However, due to their limit on the temporal resolution, transient events such as ELMs could not be resolved. These events are of particular interest as they can impose large amount of energy onto the plasma facing components in a short time scale and cause material damages. A new high speed (1.6–6.3 kHz) IR camera diagnostic has been recently installed on NSTX and has been successfully commissioned. We report technical details and first results of heat flux measurements from the diagnostic.

II. EXPERIMENTAL AND MEASUREMENT TECHNIQUE

NSTX[4,5] is a low aspect ratio tokamak ($R=0.85$ m, $a<0.67$ m, and $R/a>1.27$) with machine capabilities of $0.35<B_T<0.55$ toroidal magnetic field, $0.6<I_p<1.2$ MA plasma current, $\leq 1.2\times10^{20}$ m^{-3} central density, up to 6 MW of neutral beam injected (NBI) power and 6 MW of high harmonic fast wave heating system. NBI heating during the I_p ramp was used to minimize volt-second consumption and to extend the pulse length. H-mode plasmas are routinely accessed[6] via good wall conditions, auxiliary heating power, flexible plasma position, shape controls, etc. The density rises continuously during the H-mode phase as is typically observed in other tokamak machines.

A Santa Barbara Focalplane (SBF161) ImagIR camera with 14 bit dynamic range was recently installed on NSTX. Detectors of the camera consist of photovoltaic mercury cadmium telluride (HgCdTe) sensor operating in 8–10 μm spectral range along with camera window and lens coatings, with $128\times128/40$ μs resolution/pixel pitch. The frame rate is currently 1.6–6.3 kHz depending on the frame size with flexible integration time of 0.1 μs–3 ms for 128×128 full frame. An integrated vacuum dewar contains liquid nitrogen (LN2) to eliminate IR radiation emitted by the camera itself with hold time of longer than 10 h. Because of the geometry of the dewar, the camera must be mounted to view horizontally, requiring the implementation of an intermediate mirror mounted on top of the machine to relay the image of lower divertor tiles to the camera lens through a viewing port. Focal length of 25 mm of the front lens gives 45° of circular field-of-view (FOV) and a divertor tile image with spatial resolution of ~6.7 mm. Blackbody source calibration against the emission intensity provides a measurement of divertor surface temperature ranging from 20 to 730 °C. The noise equivalent temperature difference of the camera at LN2 temperature, reported by the camera provider, is estimated to be 17.32 mK, based on a two point nonuniformity correction measurement.

The camera has a shielded tape cable to within less than 1 cm of the focal plane array. The tape cable carries the analog signals back to a high density 37-pin micro-D connector, which is welded into the all-aluminum dewar shell's back interface plate. The analog-to-digital converter electronics board is fully enclosed in an aluminum box and is plugged directly into the 37-pin micro-D connector, thereby limiting exposure of the sensitive analog outputs to electromagnetic interference (EMI) effects. At the present mounting location, where the total magnetic field is typically estimated to be ~0.3 T, the camera hardware and the IR image are found resilient to the electromagnetic noise produced by NSTX plasma discharges.

A remote relay switch enabled power cycling of both the camera and the local control computer to reinitialize hardware when necessary. The camera has an internal digital interface unit (14 bit capability) and a PC-CamLink frame grabber board by Dalsa Coreco has been installed on the local WINDOWS computer. The camera is synchronized with experiment through an external electrical trigger to the frame grabber board. Since the trigger is aligned with the central clock cycle, it comes in at the beginning of each shot ($t=t_0$)

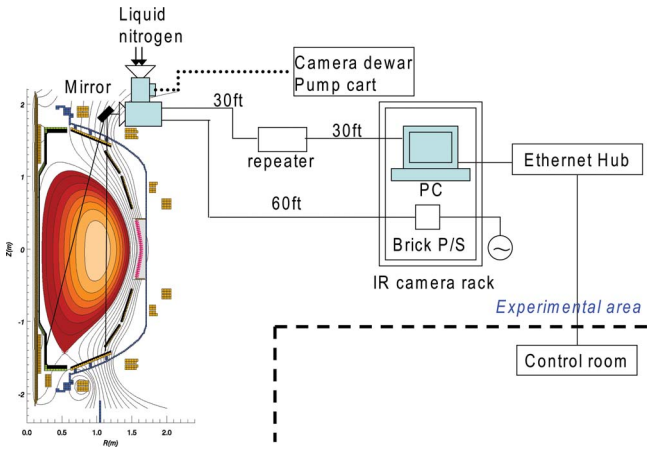

FIG. 1. (Color online) A schematic view of the installed IR camera system, viewing down the lower divertor tiles via an intermediate mirror.

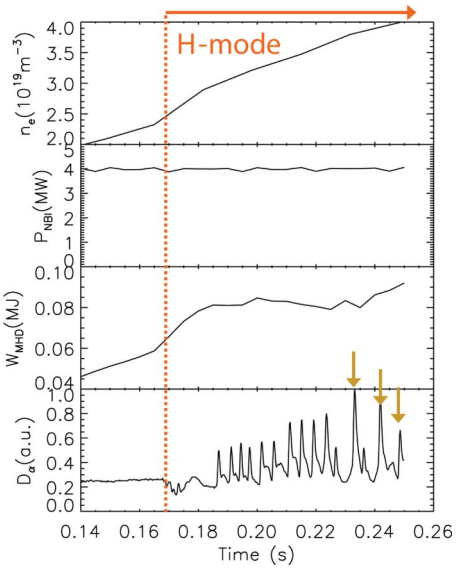

FIG. 3. (Color online) Time trace of several plasma parameters for the same time window shown in Fig. 4. Arrows in the D_α signal indicate the ELM peaks shown in Fig. 5.

and the framing starts at t_0 with a preprogrammed rate. The timing is verified by comparing the IR image with data from other diagnostics, e.g., D_α camera. The PC-CamLink can sustain 16 bit per pixel Camera Link data at over 40×10^6 pixels/s direct to PC random access memory (RAM) with 64 Mbyte of on-board RAM buffer and the standard Base Camera Link I/O lines on the Camera Link connector, plus several I/O lines on the auxiliary 15-pin connector on the back of the frame grabber.

Data acquisition is controlled by a PC application, which responds to an external trigger from the NSTX shot cycle, initializes the camera, and collects camera frames for a programmable number of frames during which the camera is in a continuous free-running acquisition mode acquiring frames at 1.6–6.3 kHz. A separate program has been written in C++ and built using VISUAL STUDIO 2005 to read the raw image files to arrange pixel intensities into a multidimensional array. The code is linked against MDSPLUS (Ref. 7) (a local data storage structure) libraries, allowing access to standard MDSPLUS functions for data access. It then connects to the NSTX MDSPLUS data server and places the array of pixel intensities as well as other relevant acquisition parameters into an MDSPLUS tree.

Figure 1 shows a schematic view showing the orientation of the camera and intermediate mirror on the torus, indicating the FOV. The schematic links between the camera and the local control computer, and between the control computer and the control room terminal are also included in the figure.

III. RESULTS OF SURFACE TEMPERATURE AND HEAT FLUX MEASUREMENT

A typical, mirror corrected, IR image of the lower divertor tiles are shown in Fig. 2. Overlaid are two sample radial slices where data analysis occurs. A series of data analysis codes was developed to convert the surface emission into temperature and then calculate the heat flux by solving the heat conduction equation. At present, fixed thermal conductivity of the ATJ graphite tiles in the NSTX divertor and a one-dimensional heat conduction model without taking account of thin surface layer effect are being used. This is the same method applied at DIII-D[8,9] and for the NSTX slow IR cameras.[1]

Figure 3 shows the time trace of various plasma parameters for an ELMy H-mode discharge for a given time win-

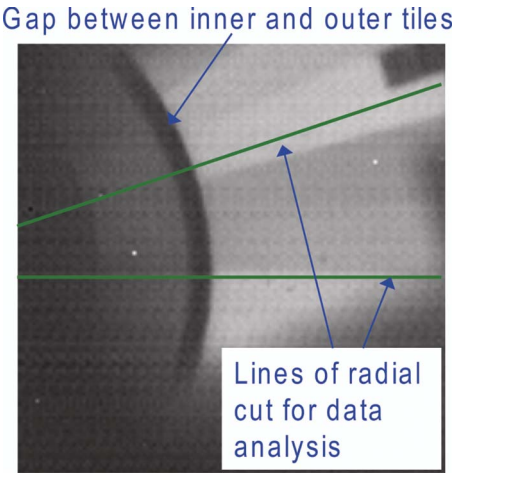

FIG. 2. (Color online) An IR image of lower divertor tiles viewing from the top of NSTX. Radial profiles of temperature and heat flux are measured along the radial cut line in either horizontal or diagonal direction.

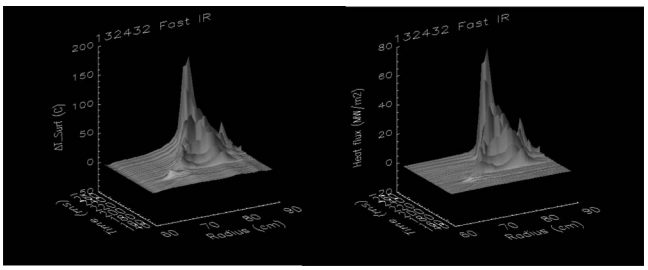

FIG. 4. Measured surface temperature (left) and heat flux (right) profiles as a function of radius and time for an ELMy H-mode plasma at frame rate of 1.6 kHz.

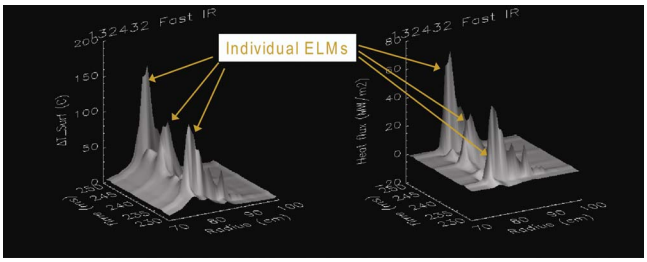

FIG. 5. (Color online) Measured surface temperature (left) and heat flux (right) profiles as a function of radius and time for individual ELMs with frame rate of 1.6 kHz.

dow. Shown in Fig. 4 are the measured surface temperature and heat flux at the outer divertor tiles as a function of radius and time for the same time window as in Fig. 3. D_α signal for the lower divertor tiles in Fig. 3 shows repetitive ELMs with short time scales, and the rapid peaks at both the temperature and heat flux profiles in Fig. 4 reflect these ELMs. Note that both the temperature and heat flux peaks from ELMs increase in time as the plasma stored energy (W_{MHD}) increases. In the later stage of the time window, the temperature increase due to an ELM approaches to 170 °C, producing heat flux density of over 70 MW/m^2. Figure 5 shows profiles in a narrower time window to examine the effect of individual ELMs in more detail. It is clearly seen that both the temperature and heat flux profiles become broadened at the moment of ELM impact with peak temperature and heat flux each increasing by a factor of ~4 and ~10, respectively. Several local peaks are also observed in both temperature and heat flux profiles during the ELM. These local peaks represent the so-called "filaments" that originate inside the separatrix in an upstream location and move out radially and are transported along the magnetic field, which impose additional heat and particle impact on the divertor tiles. The ELMs push the outer strike point out by ~1 cm momentarily. Figure 6 compares two heat flux profiles at an ELM peak and during the inter-ELM period with two images framed consecutively. It is shown that the ELM makes the peak heat flux jump almost

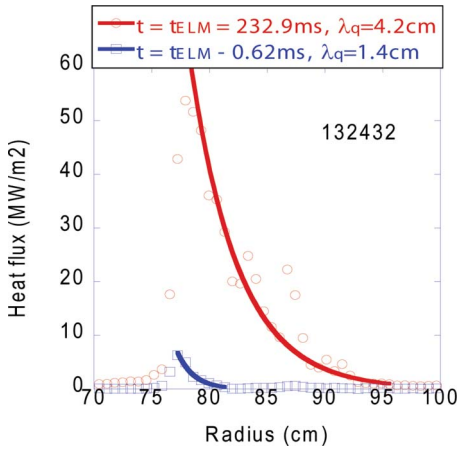

FIG. 6. (Color online) Comparison of measured heat flux profiles between ELM-peak [(dark gray (red)] and inter-ELM [light gray (blue)] periods. The frame rate was 1.6 kHz for this shot and the above profiles were obtained from two consecutive camera frames. t_{ELM} indicates time slice for the peak heat flux at the moment of ELM impact onto the tile.

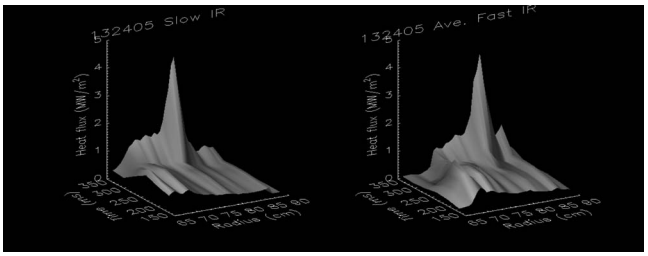

FIG. 7. Measured heat flux profiles from the slow (30 Hz) IR camera (left) and the time averaged heat flux profiles from the fast IR camera (6.3 kHz) over the frequency of 30 Hz (right), in order to compare the measurements for the same divertor location, displaced by 30° toroidally.

by a factor of 9 (from ~6 MW/m^2 to ~54 MW/m^2) and broadens the scrape-off layer (SOL) width, defined by the e-folding length in the near SOL by a factor of 3 (from 1.4 to 4.2 cm), compared with the inter-ELM profile.

In order to validate the fast IR camera measurements, a comparison with slow (framing frequency, $f_{slow}=30$ Hz) IR camera data was made for a small ELM, i.e., type-V, H-mode discharge. As this kind of discharge tends to exhaust small amount of heat flux quite constantly, rather than expels a huge heat pulse intermittently as in type-I or type-III ELMy H-mode plasmas, it provides an advantage of comparing rather smooth profiles, for both fast and slow IR data. The slow IR camera is located on the top of the machine viewing the lower divertor tiles in a different toroidal location displaced by 30° clockwise. The frame rate of the fast IR camera, f_{fast} for this discharge was chosen as 6300 Hz. The frequency of type-V ELMs observed in the IR images were approximately 1–2 kHz and therefore the slow IR camera with 30 Hz frame speed takes an average image over 30–60 ELMs for each frame, while the fast IR camera has enough temporal resolution to resolve individual ELMs. The time slices of the fast camera have been aligned with those of the slow camera and approximately 210 frames ($f_{fast}/f_{slow}=6300/30$) have been "time averaged" to generate a frame for each time slice from the slow camera. Figure 7 shows the comparison between the two cases. The two heat flux profiles are seen to agree with each other very nicely. The excellent agreement between two independent IR measurements shows the reliability of the measurement from both diagnostics. Generally, the difference in peak heat flux values when comparing results from the two diagnostics tends to be larger than the difference in the temperature because a change in temperature in a short time period produces a large heat flux change. This is particularly true when comparing data from the two diagnostics for large ELM H-mode discharges. However, taking account of the possibility of toroidal asymmetry of heat flux deposition, error bars on the temperature calibration of each camera, and the possibility of slight misalignment of timing sequences for the averaging process, the overall agreement appears very good.

IV. SUMMARY AND CONCLUSION

Heat flux measurement during the ELM peak for a regular type-III ELM reveals a highly concentrated and transient heat deposition on the lower divertor tiles, with peak heat

flux vales of 40–70 MW/m^2 and e-folding lengths of 3–4 cm in the time scale of ~0.6 ms, compared with 4–6 MW/m^2 peak heat flux and 1–1.5 cm e-folding length for the inter-ELM period. This corresponds to 3%–5% of the total stored energy out of the confined region. In order to validate the measured heat flux values, a comparison with data from the slow IR camera, taken simultaneously with the fast IR camera, was made by taking average of the data on the slow camera frame rate (30 Hz) and showed a good agreement for the same radial coverage. An upgrade to an even higher frame rate of ~20 kHz is being planned and this will enable us to collect data with temporal resolution of 50 μs, which is expected to be fast enough to measure heat flux rise time due to an ELM impact. Also, the development of a two-dimensional heat conduction model with the thin surface layer effect taken into account is in progress for the heat flux calculation.

ACKNOWLEDGMENTS

This work was supported by the U.S. Department of Energy, Contract Nos. DE-AC05-00OR22725 and DE-AC02-09CH11466.

[1] D. Mastrovito, R. Maingi, H. W. Kugel, and A. L. Roquemore, Rev. Sci. Instrum. **74**, 5090 (2003).
[2] R. Maingi, C. E. Bush, R. Kaita, H. W. Kugel, A. L. Roquemore, S. F. Paul, V. A. Soukhanovskii, and NSTX Team, J. Nucl. Mater. **363–365**, 196 (2007).
[3] V. Soukhanovskii, R. Maingi, D. A. Gates, J. E. Menard, S. F. Paul, R. Raman, A. L. Roquemore, M. G. Bell, R. E. Bell, J. A. Boedo, C. E. Bush, R. Kaita, H. W. Kugel, B. P. LeBlanc, D. Mueller, and NSTX Team, Phys. Plasmas **16**, 022501 (2009).
[4] M. Ono, S. M. Kaye, Y.-K. M. Peng, G. Barnes, W. Blanchard, M. D. Carter, J. Chrzanowski, L. Dudek, R. Ewig, D. Gates, R. E. Hatcher, T. Jarboe, S. C. Jardin, D. Johnson, R. Kaita, M. Kalish, C. E. Kessel, H. W. Kugel, R. Maingi, R. Majeski, J. Manickam, B. McCormack, J. Menard, D. Mueller, B. A. Nelson, B. E. Nelson, C. Neumeyer, G. Oliaro, F. Paoletti, R. Parsells, E. Perry, N. Pomphrey, S. Ramakrishnan, R. Raman, G. Rewoldt, J. Robinson, A. L. Roquemore, P. Ryan, S. Sabbagh, D. Swain, E. J. Synakowski, M. Viola, M. Williams, J. R. Wilson, and NSTX Team, Nucl. Fusion **40**, 557 (2000).
[5] S. M. Kaye, M. G. Bell, R. E. Bell, S. Bernabei, J. Bialek, T. Biewer, W. Blanchard, J. Boedo, C. Bush, M. D. Carter, W. Choe, N. Crocker, D. S. Darrow, W. Davis, L. Delgado-Aparicio, S. Diem, J. Ferron, A. Field, J. Foley, E. D. Fredrickson, D. A. Gates, T. Gibney, R. Harvey, R. E. Hatcher, W. Heidbrink, K. Hill, J. C. Hosea, T. R. Jarboe, D. W. Johnson, R. Kaita, C. Kessel, S. Kubota, H. W. Kugel, J. Lawson, B. P. LeBlanc, K. C. Lee, F. Levinton, R. Maingi, J. Manickam, R. Maqueda, R. Marsala, D. Mastrovito, T. K. Mau, S. S. Medley, J. Menard, H. Meyer, D. R. Mikkelsen, D. Mueller, T. Munsat, B. A. Nelson, C. Neumeyer, N. Nishino, M. Ono, H. Park, W. Park, S. Paul, T. Peebles, M. Peng, C. Phillips, A. Pigarov, R. Pinsker, A. Ram, S. Ramakrishnan, R. Raman, D. Rasmussen, M. Redi, M. Rensink, G. Rewoldt, J. Robinson, P. Roney, A. L. Roquemore, E. Ruskov, P. Ryan, S. A. Sabbagh, H. Schneider, C. H. Skinner, D. R. Smith, A. Sontag, V. Soukhanovskii, T. Stevenson, D. Stotler, B. Stratton, D. Stutman, D. Swain, E. Synakowski, Y. Takase, G. Taylor, K. Tritz, A. von Halle, M. Wade, R. White, J. Wilgen, M. Williams, J. R. Wilson, W. Zhu, S. J. Zweben, R. Akers, P. Beiersdorfer, R. Betti, T. Bigelow, M. Bitter, P. Bonoli, C. Bourdelle, C. S. Chang, J. Chrzanowski, C. Domier, L. Dudek, P. C. Efthimion, M. Finkenthal, E. Fredd, G. Y. Fu, A. Glasser, R. J. Goldston, N. L. Greenough, L. R. Grisham, N. Gorelenkov, L. Guazzotto, R. J. Hawryluk, J. Hogan, W. Houlberg, D. Humphreys, F. Jaeger, M. Kalish, S. Krasheninnikov, L. L. Lao, J. Lawrence, J. Leuer, D. Liu, N. C. Luhmann, E. Mazzucato, G. Oliaro, D. Pacella, R. Parsells, M. Schaffer, I. Semenov, K. C. Shaing, M. A. Shapiro, K. Shinohara, P. Sichta, X. Tang, R. Vero, D. Walker, and W. Wampler, Nucl. Fusion **45**, S168 (2005).
[6] R. Maingi, M. G. Bell, R. E. Bell, C. E. Bush, E. D. Fredrickson, D. A. Gates, T. Gray, D. W. Johnson, R. Kaita, S. M. Kaye, S. Kubota, H. W. Kugel, C. J. Lasnier, B. P. LeBlanc, R. J. Maqueda, D. Mastrovito, J. E. Menard, D. Mueller, M. Ono, F. Paoletti, S. J. Paul, Y.-K. M. Peng, A. L. Roquemore, S. A. Sabbagh, C. H. Skinner, V. A. Soukhanovskii, D. Stutman, D. W. Swain, E. J. Synakowski, T. Tan, J. B. Wilgen, and S. J. Zweben, Nucl. Fusion **43**, 969 (2003).
[7] MDSPLUS User Manual, http://www.mdsplus.org.
[8] H. S. Carslaw and J. C. Jaeger, *Conduction of Heat in Solids* (Clarendon, Oxford, 1959).
[9] D. N. Hill, R. Ellis, W. Ferguson, and D. E. Perkins, Rev. Sci. Instrum. **59**, 1878 (1988).